Article:
Yin, H, Lanson, B, Zhang, S et al. (12 more authors) (2022) Effect and fate of Ni during aging and thermal-induced phyllomanganate-to-tectomanganate transformation. Geochimica et Cosmochimica Acta, 333. pp. 200-215. ISSN 0016-7037

https://doi.org/10.1016/j.gca.2022.07.014

Effect and fate of Ni during aging and thermal-induced phyllomanganate-to-tectomanganate transformation

Hui Yin[1,2,*], Bruno Lanson[3], Shuang Zhang[1,2], Lu Liu[1,2], Caroline L. Peacock[4], Jeffrey E. Post[5], Mengqiang Zhu[6], Wei Li[7], Qian Wang[8], Jing Zhang[9], Yong Yang[1,2], Guohong Qiu[1,2], Xionghan Feng[1,2], Wenfeng Tan[1,2], Fan Liu[1,2,*]

[1]Key Laboratory of Arable Land Conservation (Middle and Lower Reaches of Yangtse River), Ministry of Agriculture and Rural affairs, College of Resources and Environment, Huazhong Agricultural University, Wuhan 430070, China.
[2]State Environmental Protection Key Laboratory of Soil Health and Green Remediation, Ministry of Ecology and Environment, Huazhong Agricultural University, Wuhan 430070, China.
[3]Univ. Grenoble Alpes, Univ. Savoie Mont Blanc, CNRS, IRD, Univ. Gustave Eiffel, ISTerre, F-38000 Grenoble, France
[4]School of Earth and Environment, University of Leeds, Leeds, LS2 9JT, UK
[5]Department of Mineral Sciences, NHB 119, Smithsonian Institution, Washington DC 20013-7012, USA
[6]Department of Ecosystem Science and Management, University of Wyoming, 1000 E. University Ave., Laramie, WY 82071, USA
[7]Key Laboratory of Surficial Geochemistry, Ministry of Education, School of Earth Sciences and Engineering, Nanjing University, Nanjing 210023, China
[8]School of Earth and Atmospheric Sciences, Georgia Institute of Technology, 311 Ferst Dr., Atlanta, Georgia 30332-0340, USA
[9]Beijing Synchrotron Radiation Facility, Institute of High Energy Physics, Chinese Academy of Sciences, Beijing 100039, China

Corresponding Author
[*]Tel.: +86 27 87280271. Fax: +86 27 87282163.
E-mail: yinhui666@mail.hzau.edu.cn; liufan@mail.hzau.edu.cn.

Abstract: Phyllomanganates are ubiquitous in a variety of environments and commonly enriched in transition metal elements, such as Ni. The effect of such foreign metal cations on phyllomanganate transformation is widely documented under aqueous conditions together with the induced modification of Ni geochemical behavior. A similar knowledge is lacking however on phyllomanganate transformation and on the induced fate of associated metal elements that may occur under dry conditions, that prevail in deserts and arid areas increasingly exposed to severe droughts or wildfires. The present study shows that crystallinity, morphology, Mn oxidation state, and Ni binding mechanisms are essentially unaffected when aging hexagonal birnessite (Mn oxidation state ~3.90 and Ni/Mn molar ratios of 0.00 and 0.13) in the dry state at room temperature for up to 8 years. In contrast, heating aged Ni-doped birnessite to 25-200 ^{o}C results in an increased proportion of edge-sharing Ni-Ni(Mn) pairs with increasing temperature induced by the migration of interlayer Ni to birnessite octahedral layers and/or by an increased sharing of coordination oxygens by interlayer Ni/Mn from adjacent layers. Further heating to 400 ^{o}C does not change this proportion, with birnessite layer structure being retained. Transformation of Ni-doped birnessite to cryptomelane is complete at 500 ^{o}C, while that of Ni-free birnessite is achieved at 400 ^{o}C, suggesting that Ni doping increases birnessite thermal stability. Birnessite-to-cryptomelane transformation comes with a strong increase of Mn oxidation state, whereas this parameter remains unchanged in heated birnessite samples. Ni incorporation in the cryptomelane framework, reduces its release during reductive acid dissolution by a factor of 396 ± 15 compared to initial birnessite. These results shed

light on mineral transformation affecting layered manganates under dry conditions and on the fate of associated transition metal elements.

Keywords: manganese oxide, mineral transformation, dry aging, thermal treatment, transition metals

1. Introduction

Manganese (oxyhydr)oxide minerals are widespread in geological settings such as soils, sediments, ocean nodules, and desert varnishes (Post, 1999; Lu et al., 2019). Minerals from the birnessite family are the most common naturally occurring Mn oxides and may form through both biogenic and abiotic processes (Villalobos et al., 2003; Morgan, 2005; Lanson et al., 2008). These phyllomanganates are composed of layers of edge-sharing [Mn(IV)O_6] octahedra with hydrated interlayers (Giovanoli, 1980). Existence of Mn vacancies and/or isomorphous substitutions of low valence cations such as Mn(III), Ni(II), Co(III), and Fe(III) for Mn(IV) in birnessite layers induce a net negative charge in the layers, which is compensated for by the presence of hydrated cations and/or protons in the interlayer region (Drits et al., 1997; Silvester et al., 1997). Owing to their unique structure (tiny particle sizes, vacancies, and mixed Mn valences), birnessites have strong adsorption and/or oxidation capacities for a variety of trace metals, and thus host a large number of metal cations (Peacock, 2009; Simanova and Pena, 2015). Natural birnessite minerals are generally enriched in metals such as Co, Ni, and Fe (Taylor et al., 1964; Manceau et al., 2014; Lee et al., 2019).

Birnessite-like minerals can be precursors of other naturally occurring Mn oxides such as tectomanganates. Natural cryptomelane, which has a 2×2 tunnel structure, is mainly found in supergene oxidation zones of Mn deposits, lateritic weathering profiles, and volcanic ashes, and may form through authigenic precipitation or transformation from birnessite minerals (Lu and Li, 2015). Birnessite can transform to cryptomelane via dissolution-reprecipitation pathways (Jothiramalingam et al., 2006; Zhang et al., 2011, 2016; Sinha et al., 2013) or via topotactic transformation mechanisms (Tu et al., 1994; Ching et al., 2001; Grangeon et al., 2014, 2015). It was proposed that Mn(III) content in the octahedral layers plays a key role in the conversion from phyllomanganates to tectomanganates (Atkins et al., 2014; Grangeon et al., 2014, 2015; Yang et al., 2018). Most studies investigating the phyllomanganate-to-tectomanganate transformation were conducted in solution (Tu et al., 1994; Zhang et al., 2011; Atkins et al., 2014; Yang et al., 2018, 2019; Wu et al., 2019, 2021), consistent with the prevalence of wet conditions in soils and sediments. Dry conditions prevail however in desert soils, that cover more than 20% of Earth's land area (Zhu et al., 2022), and in soils affected by seasonal droughts. As a result of the present climate change, the frequency of extreme weather patterns such as severe droughts and extreme heat events has increased over the past two decades, a long-term tendency according to climate projections (Vicente-Serrano et al., 2020). As the phyllomanganate-to-tectomanganate transformation processes even in the dry state (Atkins et al., 2014; Grangeon et al., 2014, 2015; Yang et al., 2018), it is important to investigate such mineral transformation and the fate of associated metal cations in dry conditions.

Very few studies have reported dry-state transformation over long periods of time (Grangeon et al., 2014, 2015) and, to our knowledge, no study has investigated dry-state transformation at elevated temperatures linked for example to the increasing frequency of wildfires (Murphy and Timbal, 2008). During large wildfires, soil temperature may exceed 600 ºC (Rein et al., 2008), possibly resulting in the transformation of soil minerals (Johnston et al., 2016; Li et al., 2019). In particular, laboratory experiments showed that birnessite can be thermally transformed to cryptomelane (Chen et al., 1986; Golden et al., 1986). Such transformation may significantly affect the fate of elements in the initial minerals. For example, heating As(V)-coprecipitated iron oxyhydroxysulfate mineral schwertmannite at temperatures higher than 400 ºC results in the formation of hematite and causes the initially structurally incorporated As to be surface-complexed, thus enhancing As mobilization (Johnston et al., 2016). Similar processes have also been reported for transformation of naturally occurring goethite-rich materials upon heating (Perrier et al., 2006; Landers et al., 2009). However, no studies have yet investigated the fate of metal elements associated with Mn oxide minerals during their thermal-induced transformation.

The present study thus investigates the possible phase transformation affecting Ni-doped hexagonal birnessites during aging in the dry state at room temperature for 5 and 8 years and subsequent heating over a wide range of temperatures (50-500 ºC) and the induced fate of associated Ni. Powder X-ray diffraction, electron microscopies, thermogravimetric analysis, and Ni and Mn K-edge X-ray absorption fine structure spectroscopy are combined with acid dissolution experiments for this purpose. Nickel

was chosen as a model metal cation because of being 1) one important trace metal nutrient and contaminant, 2) a redox-insensitive element, and 3) because its binding mechanisms on birnessite-like minerals have been thoroughly studied in the literature. The present results provide insights into the mobility and bioavailability of metal nutrients and contaminants associated with the phase changes of host Mn oxide minerals, and may deepen our understanding of Mn-mediated metal geochemical behaviors in dry soils and during extreme heating events.

2. Materials and methods

2.1 Dry aging of Ni-doped birnessites at room temperature

Hexagonal birnessite, HB, and Ni-doped birnessite, Ni10, from our previous study (Yin et al., 2012) were used here. These samples were synthesized according to the protocol of McKenzie (1971). Briefly, this protocol involves the reduction of a boiling $KMnO_4$ solution (300 mL, 0.667 M) by an HCl solution (45 mL, 6 M) in the absence/presence of $NiCl_2$ (Ni/Mn molar ratio of 0.10). The pHs of the synthetic suspensions after mineral crystallization were ~7.2 and ~5.5, respectively. After washing thoroughly the obtained solids, they were dried at 40 ^{o}C for several days, ground carefully to particle sizes below 100 mesh, and reserved for further use. HB and Ni10 samples have specific surface areas (SSAs) of 19 and 71 $m^2 \cdot g^{-1}$, respectively (Yin et al., 2012). The Ni content in Ni10 is 6.1 wt.%, and the K contents in HB and Ni10 are 8.4 and 3.8 wt.% respectively (Yin et al., 2012).

Aliquots of these birnessite powders were stored in sealed polystyrene tubes and kept in the dark at room temperature. After aging for 5 and 8 years, some of the samples

were thoroughly characterized. As-obtained, aged samples were correspondingly named as HB_Ny and Ni10_Ny (N = 5 or 8; Table 1).

2.2 Thermal treatment of the 8-year aged samples

In addition, the 8-year aged samples (HB_8y and Ni10_8y) were heated to temperatures (50, 100, 150, 200, 300, 400 and 500 ºC), spanning the common range of soil temperatures reported during wildfires (Rein et al., 2008). Typically, ~0.1 g of each sample was placed in a ceramic crucible and heated in a muffle furnace in air. After increasing the furnace temperature to the set value (rate of 10 $^{o}C \cdot min^{-1}$), the sample powder was kept at this temperature for 2 h, consistent with previous studies (Cai et al., 2001). The furnace door was then opened to let the powder cool down naturally to room temperature, and as-obtained solids were stored for further analysis. These samples were labelled HB_8y_T and Ni10_8y_T, where T stands for the temperature used in ºC (Table 1).

2.3 Solid characterization

Powder X-ray diffraction (XRD) analysis was used to identify structural changes of Mn oxide samples. Data were collected on a Bruker D8 Advance diffractometer. As the XRD profile changes during drying aging at room temperature were expected to be minimal, the diffraction data of the 5- and 8-year aged samples were collected at a step size of 0.04 º2θ Cu Kα using a counting time of 10 or 40 sec per step. The XRD data of the thermal transformation products were collected using a scanning rate of 10º per min with a step size of 0.02 º2θ. Field emission scanning electron microscopy (FESEM) images of the samples were obtained using a Jeol JSM-6700F microscope after coating

133 the minerals with a gold evaporated film for 30 s. High angle annular dark field
134 (HAADF) scanning transmission electron microscopy (STEM) images of Ni10_8y_500
135 were obtained by a JEOL JEM-ARM200F microscope equipped with a spherical
136 aberration correction system. Thermogravimetric analysis (TGA) of the Ni-doped
137 birnessites before and after 8-year aging was conducted from ~35 ºC to 800 ºC on a
138 NETZSCH TG 209 thermal analyser in N_2 or dry air at a flow rate of 20 mL·min^{-1} with
139 a heating rate of 10 ºC·min^{-1}.

140 **2.4 X-ray absorption fine structure (XAFS) spectra**

141 The XAFS spectra were measured at room temperature on the 1W1B beamline at
142 the Beijing Synchrotron Radiation Facility (Yin et al., 2012, 2015). Ni K-edge data
143 were obtained in fluorescence mode over the 8157-9063 eV range. Monochromator
144 energy was calibrated using a Ni metal foil (E_0 = 8333 eV). Mn K-edge data were
145 collected in transmission mode over the 6363-7311 eV range for most samples (6340-
146 7104 eV for 8-year aged HB and Ni10 samples heated to 50 and 150 ºC). A Mn metal
147 foil was used to calibrate the monochromator (E_0 = 6539 eV).

148 Data reduction and analysis were performed using Ifeffit/SIXPack (Ravel and
149 Newville, 2005; Webb, 2005). Parameters used for background removal of Ni K-edge
150 spectra were: E_0 = 8343 eV, Rbkg = 1.0 Å and k-weight = 2. After background removal
151 and normalization, spectra were converted into the k^3-weighted functions and Fourier
152 transforms (FTs) were calculated over 2.8-12.5 Å^{-1} (k range) and 1-6 Å (R range),
153 respectively. Mn K-edge spectra were background-subtracted using the following
154 parameters: E_0 = 6553 eV, Rbkg = 1.0 Å and k-weight = 2. XAFS spectra were then

converted into the k^3-weighted functions, and FTs were calculated over 3.4-12.1 $Å^{-1}$ and 1-4 Å (k and R ranges, respectively). Structural parameters (distance, R; coordination number, CN; and Debye-Waller factor, σ^2) for Ni local environments were obtained by fitting the experimental k^3-weighted EXAFS spectra to the standard EXAFS equation (Kelly et al., 2008) using several single-scattering paths, as described previously (Peña et al., 2010; Yin et al., 2012). Phase and amplitude functions for single-scattering paths were calculated using FEFF7 (Rehr et al., 1992). Clusters of atoms used for the analysis of Ni K-edge EXAFS spectra were based on chalcophanite crystal structure (Post and Appleman, 1988) and substituting Ni for interlayer Zn or layer Mn. An amplitude reduction factor (S_0^2) of 0.848 was adopted for Ni, consistent with our previous study (Yin et al., 2012).

To determine the relative proportions of heterovalent Mn cations (Mn^{4+}, Mn^{3+} and Mn^{2+}) in Mn oxides, Mn K-edge XANES spectra were analyzed using the Combo method (Manceau et al., 2012). In a typical procedure, the 17 standard spectra used to develop the method (Table S1) were first imported. 4-8 references with non-negative fractions were then used for the linear combination fitting of normalized XANES spectra. Mn K-edge EXAFS data were fitted using birnessite (Grangeon et al., 2010) or cryptomelane (Yin et al., 2015) model. An amplitude reduction factor (S_0^2) of 0.973 was adopted from our previous study (Yin et al., 2014).

In all EXAFS fits, the number of independent variables used was smaller than the number of independent data points. During Fourier transform and EXAFS data fitting, a Hanning window was used.

177 **2.5 Acid dissolution experiments**

178 Consistent with previous studies (Beak et al., 2008; Qin et al., 2017) acid
179 dissolution experiments were performed to investigate Ni crystal chemistry, stability,
180 and bioaccessibility in these samples. Briefly, 0.0400 g of solid were dissolved at 37 ºC
181 in 250 mL of 2 M HCl solution while stirring at a constant rate. These conditions are
182 similar to *in vitro* measurements of metal bioaccessibility in the gastric phase (Beak et
183 al., 2008). Suspension aliquots (5 mL) were withdrawn at predetermined intervals and
184 filtered immediately through 0.22 μm membrane filters. The concentrations of Mn^{2+}
185 and Ni^{2+} in the filtrate were analyzed using atomic absorption spectrometry (AAS,
186 Varian AAS 240FS). The metal (Me) dissolution ratio was calculated as χ_{Me} =
187 Me(t)/Me(total), where Me(t) is the aqueous metal concentration at time t, and Me(total)
188 is the final metal concentration after complete dissolution of the solid.

189 **3 Results**

190 **3.1 Changes in mineralogical phases**

191 Powder XRD patterns of the Ni-doped birnessite samples before and after dry
192 aging at RT for 5 and 8 years (Fig. 1a,b) are typical for turbostratic hexagonal
193 birnessites, and can be indexed using a C-centered two-dimensional unit cell (Drits et
194 al., 1997, 2007). The unsplit (31, 02) bands and the ratios of (11, 20) to (31, 02) d values
195 close to √3 both confirm the hexagonal layer symmetry (Drits et al., 2007). XRD
196 profiles of aged samples show only minimal differences with those of fresh samples.
197 For both HB and Ni10 samples, the position of the (31, 20) diffraction band shifts
198 slightly towards lower angle for the 8-year aged sample compared to fresh and 5-year

aged samples, indicating a slight increase of the layer lattice parameter b, without significant distortion of the hexagonal layer symmetry however (Grangeon et al., 2008). Consistent with the high values of Mn average oxidation state in the initial products (3.86 and 3.95 for HB and Ni10, respectively – Yin et al., 2012), similarity of the XRD profiles of fresh and aged samples supports the stability of birnessite layer and interlayer structures and the stability of these minerals in the dry state at room temperature.

Upon heating, powder XRD patterns of the 8-year aged samples undergo significant changes (Fig. 1c,d). When heated to temperatures ≤ 300 ºC, all samples essentially retain their layer structure. After heating to 400 ºC, HB_8y is fully transformed to cryptomelane ($K(Mn^{4+}{}_7Mn^{3+})O_{16}$ – ICDD 74-1451), while Ni10_8y retains most of its layer structure, being only partly transformed to cryptomelane. After heating to 500 ºC for 2 h, Ni10_8y is essentially transformed to cryptomelane, with a minor $NiMn(IV)O_3$ (ICDD 75-2089) impurity. Further linear combination fitting (LCF) analysis of Mn K-edge EXAFS spectra of thermal transformation products of HB_8y and Ni10_8y by using spectra of Ni10_8y_300 and HB_8y_500 as birnessite and cryptomelane standards, respectively, confirms the XRD results. For example, LCF analysis shows that Ni10_8y_400 is composed of 87 ± 1% birnessite and 13 ± 1% cryptomelane (Fig. S1 and Table S2).

3.2 Thermal stability of 8-year aged birnessites in N_2 or dry air

Eight-year aged birnessites are more stable than their fresh counterparts upon heating in N_2 atmosphere, although weight losses occur almost at the same temperatures

221 (Fig. 2 and Table S3a). The amount of physisorbed water is identical in HB and HB_8y
222 (35-150 °C – 8.8-9.3%), while that in Ni10_8y (35-180 °C – 11.0 ± 0.3 %) is slightly
223 lower than that in Ni10 (12.0 ± 0.1 %). The amount of structural water (150-700 °C),
224 including hydroxyl groups and interlayer water molecules (Lee et al., 2007; Yin et al.,
225 2012), is significantly lower in aged birnessites (4.8 ± 0.5 % and 5.8 ± 0.4 % in HB_8y
226 and Ni10_8y, respectively) compared to corresponding fresh samples (7.5 ± 0.9 % and
227 7.2 ± 0.2 %).The weight losses assigned to lattice oxygen (700-800 °C) are alike in HB
228 and HB_8y (4.3 ± 1.0 % and 3.8 ± 0.5 %, respectively). Contrastingly, this weight loss
229 is lower in Ni10_8y (4.1 ± 0.2 %) compared to Ni10 (7.5 ± 0.5 %). The lattice oxygen
230 weight loss is related to Mn(IV) reduction and formation of phases such as Mn_2O_3 (Lee
231 et al., 2007).

232 The profiles for the release of both physisorbed and structural water molecules
233 from the 8-year aged samples upon heating in air are similar to those in N_2 (Fig. 2b and
234 Table S3b). With increasing temperature, a weight increase is observed however for
235 both HB_8y (460-800 °C – 0.4 ± 0.6%) and Ni10_8y (520-660 °C – 1.0 ± 0.3%). These
236 weight gains are likely due to the oxidation of low valence $Mn^{2+/3+}$ by O_2 (Tang et al.,
237 2014). Weight loss occurs again from 660 °C for Ni10_8y, owing to the Mn reduction
238 and lattice O loss during thermal decomposition to phases such as Mn_2O_3 (Tang et al.,
239 2014). These results are consistent with previous studies that indicate oxidation of
240 $Mn^{2+/3+}$ at intermediate temperatures in air and reductive decomposition of MnO_2 at
241 high temperatures both in air and N_2 (Lee et al., 2007; Tang et al., 2014).

242 **3.3 Morphology changes**

After aging for 8 years, birnessite morphology, 3D hierarchical microspheres composed of 2D disk-like plates, changes little, with the thickness of platy crystals remaining also unchanged (Fig. 3). Heating HB_8y up to temperatures ≤ 300 ºC slightly decreases microsphere size however, and even more so plate thickness (Figs. S2-4). HB_8y_400 particles appear as prisms, consistent with the transformation to cryptomelane. This morphology is different from commonly reported needles (Sinha et al., 2013; Grangeon et al., 2015; Zhang et al., 2016), but similar to that of cryptomelane obtained from thermal transformation of triclinic birnessite (Chen et al., 1986). After heating HB_8y further to 500 ºC, cryptomelane prismatic crystals grow in all three dimensions compared to HB_8y_400. Similar to the corresponding fresh crystals, Ni10_8y crystals are smaller than HB_8y ones (Fig. 3, Figs. S2-4). Heating Ni10_8y to temperatures ≤ 400 ºC, modifies crystal size and plate thickness only marginally. Although powder XRD analysis shows a minor amount of cryptomelane in Ni10_8y_400, no prismatic crystals were observed, whereas Ni10_8y_500 consists mainly of prismatic crystals (Fig. 3g). Both the HAADF-STEM image and the corresponding Fast Fourier transform (FFT) pattern obtained on a prismatic Ni10_8y_500 crystal confirm the nature of these crystals exhibiting cryptomelane [200] facets with a *d* spacing of 4.98 Å (Fig. 3h). Atomic image (Fig. 3i) shows the 2×2 tunnels of the cryptomelane framework. In this image, the uniform dark stripes represent the K atoms and the coordinated water molecules rather than Ni in the interlayer regions. This indicates that Ni is most likely structurally incorporated in the cryptomelane framework rather than adsorbed in tunnels and/or to crystal surface.

3.4 Changes in Mn Average Oxidation State (AOS)

Manganese K-edge XANES analysis using the Combo method (Manceau et al., 2012) shows that upon dry aging, the proportion of low valence Mn ($Mn^{3+/2+}$) increases only slightly at the expense of Mn^{4+} (Fig. 4 and Table S1). Mn AOS values calculated for HB_8y and Ni10_8y (3.81 and 3.90, respectively) are similar to those of HB and Ni10 (Yin et al., 2012), within the accuracy (±0.04) of the method (Manceau et al., 2012). As birnessite Mn AOS is a key parameter for their reactivity towards various redox reactions (Wang et al., 2018), this similarity suggests that aged birnessites can effectively mediate the geochemical behavior of various redox-sensitive contaminants in the environment.

Heating of HB_8y and Ni10_8y modifies the relative proportions of various Mn species depending on temperature. Below 300 ºC, the proportions of heterovalent Mn cations in HB_8y and Ni10_8y are essentially constant whereas increasing temperature to 400 ºC for HB_8y and 500 ºC for Ni10_8y induces the oxidation of low-valence Mn cations to Mn^{4+} (Fig. 4). Consistently, Mn AOS values calculated for HB_8y heated to 50-300 ºC range 3.81-3.84, and increase to 3.91-3.93 after heating to temperatures ≥ 400 ºC. Similarly, Mn AOS values calculated for Ni10_8y heated to 50-150 ºC remain constant at 3.89-3.91. When heating Ni10_8y further to 200-400 ºC, Mn AOS values decrease to 3.82-3.85, most likely owing to Mn^{4+} reduction. Over this temperature range, the weight loss due to hydroxyl groups probably results also in the loss of oxygen anions and thus in the reduction of high valence Mn cations. Contrasting evolutions of Mn AOS observed for HB_8y and Ni10_8y over this temperature range are probably

ascribed to the larger loss of hydroxyl groups in Ni10_8y compared to HB_8y, possibly because of the lower crystallinity of the former (Fig. 1a,b and Fig. 2b). At 500 °C, the content of low valence Mn in Ni10_8y_500 is greatly decreased, and its Mn AOS is sharply increased to 3.98. The increase in Mn AOS at 400-500 °C is most likely due to the oxidation of low valence Mn by O_2 in the air, consistent with TGA results (Tang et al., 2014). In the latter case, weight gain related to absorption of O_2 by these samples occurs at 460-520 °C however, most likely owing to the steady temperature increase rate (Fig. 2b). Such an increase of Mn AOS after the birnessite-to-cryptomelane transformation is consistent with previous reports (Cai et al., 2001; Birkner and Navrotsky, 2017).

3.5 Changes in local atomic environments of Mn

Consistent with the results of powder XRD analysis, dry aging at room temperature changes little the birnessite layer structure. Similarly, upon heating to temperatures ≤ 300 °C, the k^3chi(k) functions and corresponding FTs (light gray bands in Fig. 5a,c) remain essentially unchanged, confirming the birnessite structure of heated HB_8y samples. After heating to 400 °C, the shape of the oscillation at 7.2-9.8 $Å^{-1}$ (k^3chi(k) function) changes to match that of cryptomelane (Yin et al., 2015) and the magnitude of the third peak (R + ΔR ~ 3.1 Å) in the corresponding FT is greatly increased, confirming the transformation of birnessite to cryptomelane. The oscillation profile and FT of Ni10_8y (light gray bands in Fig. 5b,d) indicate the same mineralogical evolution after heating to 500 °C.

Fittings of the Mn K-edge EXAFS spectra for heated birnessite samples based on

a birnessite structure model, and on a cryptomelane structure model for HB_8y_400, HB_8y_500, and Ni10_8y_500, provide good agreements (Fig. 5 and Table S4). All Mn-O distances in the [MnO_6] octahedra of birnessite and cryptomelane are similar at 1.904 ± 0.001 Å (n = 17) and 1.895 ± 0.001 Å (n = 3), respectively. Edge-sharing Mn-Mn distances in birnessite derived from HB (2.881 ± 0.002 Å; n = 8) are slightly longer than those derived from Ni10 (2.876 ± 0.003 Å; n = 9) at an α significance level of 0.05 (t-test). These longer distances are likely related to the higher content of layer Mn(III) in birnessite derived from HB compared to those derived from Ni10 (Fig. 4 and Table S1). Edge-sharing Mn-Mn distances in cryptomelane (2.885 ± 0.003 Å; n = 3) are statistically independent of the precursor and are slightly larger than those in birnessite layers (2.878 ± 0.004 Å; n = 17).

Significant changes are observed for the distances between interlayer Mn(Ni) to the nearest layer Mn(Ni) (Me^E-Me^{TC}; Me = Mn, Ni) (Fig. 6a and Table S4). HB_8y, Ni10_8y and layered (birnessite) samples derived from them all exhibit similar Me^E-Me^{TC} distances (3.48-3.52 Å – Fig. 6b), consistent with values reported for hexagonal birnessites (Grangeon et al., 2010). This distance is significantly decreased to 3.44-3.45 Å for cryptomelane (Fig. 6c), consistent with previous studies (Lee et al., 2007; Yin et al., 2015). Shortening of Me^E-Me^{TC} distances in cryptomelane compared to phyllomanganates is consistent with the higher proportion of Mn^{4+} cations in the former.

3.6 Evolution of Ni binding mechanisms in the mineral

Nickel K-edge k^3chi(k) oscillations and corresponding FTs of Ni10 and Ni10_8y are similar, indicating similar Ni local environments (Fig. 7). In the FTs, three main

peaks located at R+ΔR ~ 1.6 Å, ~2.4 Å and ~3.0 Å mainly correspond to the first Ni-O pair in [NiO_6] octahedron, edge-sharing Ni-Ni(Mn) pair (Ni^E) and triple corner-sharing pairs between interlayer Ni(Mn) and layer Ni(Mn) (Ni^{TC} – Peacock, 2009; Peña et al., 2010; Yin et al., 2012). Intensity ratios of these three peaks are constant indicative of similar proportions of Ni^E and Ni^{TC} (Fig. 7 and Table 2). In Ni10_8y, 74 ± 4% of the Ni content is located above/below vacant layer sites, which is statistically equivalent to Ni10 (Yin et al., 2012).

The k^3-weighted Ni K-edge EXAFS functions of heated Ni10_8y samples exhibit significant changes (Fig. 8A). Upon heating, oscillations at ~ 7.6 $Å^{-1}$ and ~ 8.2 $Å^{-1}$ are gradually combined into one oscillation and a shoulder at ~ 6.6 $Å^{-1}$ increases in intensity. The corresponding FTs (Fig. 8B) indicate that these evolutions are related to the reversing of Ni^E and Ni^{TC} peak relative intensities. Quantitative fitting indicates Ni^E proportions of 27 ± 4 %, 34 ± 5 %, 37 ± 5 %, 48 ± 5 %, 48 ± 7 %, and 51 ± 10 % for Ni10_8y samples heated to 50, 100, 150, 200, 300, and 400 ºC, respectively (Table 2).

3.7 Increased Ni stability during acid dissolution

Acid dissolution experiments were conducted to detect possible modifications of Ni availability in heat-treated Mn oxides (Fig. 9). For Ni10_8y and Ni10_8y_200, Ni^{2+} and Mn^{2+} release rates in solution are large over the first few hours. With time, the metal release rates are gradually reduced till complete dissolution, because of the lower pool. In both samples, Ni^{2+} and Mn^{2+} releases are concurrent but Ni^{2+} is released slightly faster than Mn^{2+}, consistent with the predominance of Ni^{TC}. Compared to Ni10_8y, the releases of Ni^{2+} and Mn^{2+} from Ni10_8y_200 are slower. ~99% of both Ni^{2+} and Mn^{2+}

are released after 5 and 7 h for Ni10_8y and Ni10_8y_200, respectively, possibly as a result of a minor crystal growth. Ni10_8y_500 dissolution is much slower as 50 days are needed to achieve complete dissolution. Transformation of the initial birnessite to cryptomelane is the most likely hypothesis for such a dramatic decrease of dissolution rate. In addition, Ni^{2+} and Mn^{2+} releases are not concurrent any more, Mn^{2+} being released to solution much faster than Ni^{2+}.

Nickel and Mn release kinetic curves can be fitted using the Kabai equation, $\chi_{Me}=1-\exp(-(kt)^{\alpha})$, where k and α are coefficients related to the dissolution rate constant and the mineral structure, respectively (Fig. 9 – Kabai, 1973; Kaur et al., 2010). Parameters k for both Ni^{2+} and Mn^{2+} dissolution are steadily decreasing with increasing temperature. Ni and Mn release rates measured for Ni10_8y_200 are 67 ± 4% and 71 ± 3% those from Ni10_8y, respectively. Ni and Mn release rates measured forNi10_8y_500 are dramatically reduced to 0.25 ± 0.01% and 1.51 ± 0.06% of those from Ni10_8y, respectively.

The χ_{Ni}-χ_{Mn} curves obtained for Ni10_8y and Ni10_8y_200 follow the 1:1 line with a slight convexity however (Fig. 9d), and are essentially similar to that of the fresh Ni-doped birnessite (Qin et al., 2017). This suggests a uniform Ni distribution in these birnessite samples (Alvarez et al., 2006, 2007), consistent with elemental mapping (Fig. S5). Contrastingly, the χ_{Ni}-χ_{Mn} curve obtained for Ni10_8y_500 differs significantly from the previous two exhibiting a strong concavity, indicative of Ni location in the inner parts of cryptomelane framework (Alvarez et al., 2006, 2007).

4 Discussion

375 4.1 **Stability of (Ni-doped) birnessite during aging in dry state**

376 When aged in the dry state at room temperature for up to 5 and 8 years, the
377 structure and properties of investigated Ni-free and Ni-doped hexagonal birnessites are
378 almost unchanged, preserving their hexagonal layer symmetry, morphology and Mn
379 AOS. This suggests that layered Mn oxides such as birnessite may not as unstable as
380 previously thought (Grangeon et al., 2014, 2015). Increased birnessite stability
381 observed in the present study is most likely related to their low content of Mn^{3+} as
382 previously discussed for the conversion of δ-MnO_2, a poorly crystalline analogue of
383 birnessite, to cryptomelane under similar experimental conditions (Grangeon et al.,
384 2014, 2015), possibly reinforced by larger crystal sizes. Layer Mn(III) in
385 phyllomanganates plays indeed a key role in the phyllomanganate-to-tectomanganate
386 transformation (Cui et al., 2009; Atkins et al., 2014; Grangeon et al., 2014; Yang et al.,
387 2018). Mn(III) contents of HB and Ni10 range 0.05-0.06 (Yin et al., 2012), much lower
388 than those (0.30) of the reacting δ-MnO_2 of Grangeon et al. (2014). Increased crystal
389 size of the present birnessites compared to δ-MnO_2 used by Grangeon et al. (2014)
390 likely reinforces phyllomanganate stability. Crystals with small particle sizes generally
391 have high total free energy indeed and are thus prone to phase transformation (Luo et
392 al., 2008; Navrotsky et al., 2008). Theoretically, stability of hexagonal turbostratic
393 birnessite should thus be more stable than δ-MnO_2, owing to its larger crystallite sizes.
394 Powder XRD patterns of our Ni-doped birnessites have strong (00*l*) reflections (Fig.
395 1a,b) that are absent in those of δ-MnO_2, suggesting a larger number of layers stacked
396 coherently along the **c***-axis. Further, the physical sizes of the present birnessite plates

(diameters of 100-300 nm) are also much larger than those of the vernadite samples (mean diameter of ~10 nm – Yin et al., 2012; Grangeon et al., 2015).

Subject to a similar (micro-)structure, birnessite may thus be stable in arid environments such as upland soils and rock surfaces in deserts and represent a long-term sink for trace metal elements. Dark coatings commonly found on the upper surfaces of rocks in arid and semiarid regions, such as Gobi deserts in China and Mongolia and in karst areas, are identified to be mainly composed of birnessite (Lu et al., 2019), consistent with birnessite stability observed in our aging experiments. In the present study, birnessites were aged in the dark with limited O_2 in sealed tubes. On the other hand, rock surfaces exposed to both sun light and air, and birnessite from varnishes and coatings may undergo additional evolution keeping their layer structure anyhow. Field and laboratory studies have evidenced the reductive dissolution of birnesssite under photo illumination of aqueous suspensions however (Sunda and Huntsman, 1994; Kim et al., 2012; Liu et al., 2021), consistent with theoretical calculations (Sherman, 2005; Kwon et al., 2009). Further investigation is needed to assess birnessite stability of birnessites under dry light condition and underlying mechanisms at play.

4.2 Enhanced thermal stability of birnessite by Ni doping

The present results clearly suggest that Ni doping hampers the thermal-induced transformation of birnessite to cryptomelane, although thermodynamically favored. This mineral transformation may be affected by the presence of foreign cations into the birnessite structure however (Birkner and Navrotsky, 2017). It was for example

419 reported that Cu^{2+} adsorption impedes Mn^{2+}-induced transformation of vernadite to
420 other Mn oxides at room temperature, ascribing the increased stability to the decrease
421 of mineral surface energy induced by cation adsorption (Yang et al., 2019). Ni^{2+}
422 adsorption on and affinity for birnessite surfaces are similar to those of Cu^{2+} (Kwon et
423 al., 2013; Manceau and Steinmann, 2021) and decrease of Ni-doped birnessite surface
424 energy likely contributes to its stability upon thermal treatment. Mn(III) content may
425 also play an important role for birnessite thermal transformation as reported in aqueous
426 (Cui et al., 2009; Atkins et al., 2014; Yang et al., 2018) and dry conditions (Grangeon
427 et al., 2014, 2015). Consistently, Ni doping decreases birnessite Mn(III) content (0.06
428 and 0.10 in Ni10_8y and HB_8y, respectively – Table S1) and thus increases its thermal
429 stability. Contrastingly, metal doping can significantly decrease birnessite particle size
430 (Yin et al., 2012, 2013), thus increasing its total free energy, and easing its mineralogical
431 transformation (Luo et al., 2008; Navrotsky et al., 2008). After Ni doping, birnessite
432 crystallinity was greatly reduced. The temperature for the transformation of our Ni-
433 doped birnessite to cryptomelane (500 ^{o}C) is lower than those reported for the
434 transformation of well crystallized samples (Chen et al., 1986; Golden et al., 1986; Cai
435 et al., 2001). In addition to its lower Mn(III) content, the increased stability of
436 Ni10_8y compared to HB_8y may be related to the overall decrease in the mineral total
437 free energy induced by Ni^{2+} adsorption on the vacancies and/or edges. Foreign cation
438 adsorption thus appears to increase birnessite stability and could be a key factor for
439 phyllomanganate stability in natural environments (Yang et al., 2019).

440 **4.3 Changes in Ni binding environments during thermal treatment**

441 Nickel K-edge EXAFS fitting of Ni10_8y samples after heating to 25-400 ºC
442 evidences changes in Ni crystal chemistry. Increasing temperature from 25 ºC to 200
443 ºC, increases linearly the proportion of edge-sharing Ni-Ni(Mn) pairs (R^2 = 0.9502, n
444 = 5, α = 0.05; Fig. 10A), suggesting migration of interlayer Ni cations to the octahedral
445 layer. Such rearrangement of cation configuration was previously observed during Ni^{2+}
446 adsorption on hexagonal birnessites when increasing reaction pH (Peacock, 2009; Peña
447 et al., 2010; Sorensen et al., 2020) and confirmed by density functional theory
448 calculations (Peña et al., 2010; Kwon et al., 2013). In the present study, heating can
449 provide the energy to overcome the energy barrier for this transformation, increasing
450 temperature then favoring the transformation. After heating to 200 ºC, the proportion
451 of total Ni incorporated in birnessite octahedral layers, increases from 0.26 ± 0.04 in
452 Ni10_8y to 0.48 ± 0.05 in Ni10_8y_200 (1-f value – Table 2). Increasing the
453 temperature above 200 °C does not promote further Ni migration into birnessite
454 octahedral layers however, possibly because remaining "interlayer" Ni cations sit on
455 layer edge sites by forming double corner-sharing complexes, which possess a similar
456 Ni-Mn distance of ~3.5 Å (Manceau et al., 2007).

457 Alternatively, the increased proportion of edge sharing Ni-Ni(Mn) pairs upon
458 heating may result from the loss of the interlayer water molecules and subsequent
459 rearrangement of adjacent layers. d-spacing of Ni10_8y first peak upon heating steadily
460 decreases from birnessite (001) to cryptomelane (110) peak (Fig. 10B). Loss of
461 interlayer water molecules decreases birnessite layer-to-layer distance (Fig. 6b),
462 possibly allowing triple corner-sharing Ni and Mn atoms from adjacent layers to share

their coordination O atoms owing to sample turbostratism (systematic random stacking of adjacent layers along the **c***-axis) and creating local tunnel-like domains (Fig. 6c) (Grangeon et al., 2014). TGA data obtained for Ni10_8y in air consistently indicates a significant loss of water molecules over the 35-200 ºC range (Fig. 2b), rearrangement of adjacent layers being also favored by increasing temperature. Both effects allow more coordination O atoms to be shared by interlayer Ni/Mn from adjacent layers. Departure of interlayer water molecules over the 35-200 ºC range is consistent with previous reports indicating the departure of nonstructural water molecules (sorbed to mineral surfaces) at temperatures ≤ 80-100 ºC, and of interlayer water molecules from 80-100 ºC to 205-250 ºC (Villalobos et al., 2003; Zhu et al., 2012; Grangeon et al., 2014). Though TGA analysis indicates further loss of hydroxyl groups and interlayer water molecules during heating at 180-520 ºC (Fig. 3b and Table S3b), the proportions of edge-sharing Ni-Ni(Mn) pairs are almost stable over this temperature range, the sample keeping its birnessite structure (Fig. 10A and Fig. 1d). Only when the heating temperature is increased to 500 ºC, Ni10_8y is totally transformed to cryptomelane (Fig. 1d).

4.4 **Mechanisms for enhanced Ni stability during acid dissolution**

Along birnessite transformation to tectomanganates such as todorokite and nsutite incorporated foreign metal cations are released to solution to a large extent (Tu et al., 1994; Zhang et al., 2011; Atkins et al., 2014, 2016; Yang et al., 2018, 2019; Wu et al., 2019, 2021). These studies were conducted in aqueous solutions however, and no study is available on the fate of incorporated foreign metal cations during mineral

transformation occurring in the dry state. The present study shows that long-term aging in dry state does not significantly modify Ni binding mechanisms to birnessite and thus its availability. On the contrary, thermal treatment of aged Ni-doped birnessite significantly reduces Ni availability along reductive acid dissolution of the mineral matrix. Although heated solids retain their layer structure at temperatures < 500 °C, Ni^{2+} release rate is gradually reduced with increasing temperature (Fig. 9). After heat-treatment to temperatures ≥ 500 °C, birnessite is transformed to cryptomelane and Ni^{2+} release rate is decreased by 99.75 ± 0.01% compared to the initial aged birnessite. Dissolution of Mn oxides in HCl solutions involves protonation, complexation, and reductive dissolution, with reductive dissolution by Cl^- being most efficient (Qin et al., 2017). Under similar conditions (H^+ and Cl^- concentrations, temperature, stirring rate), mineral structure, microstructure, and crystal chemistry may further influence dissolution rate. Although poorly crystalline minerals usually dissolve more readily than their highly crystalline counterparts (Liu et al., 2019), Ni^{2+} release rates are reduced for Ni10_8y_200 compared to Ni10_8y despite powder XRD and SEM analysis being indicative of Ni10_8y higher crystallinity and larger particle size. Ni binding to the birnessite structure is thus likely responsible for the lower dissolution rates of Ni10_8y_200. At temperatures ≤ 400 °C, increased proportion of edge-sharing Ni-Ni(Mn) pairs (Fig. 10A), that may result both from Ni migration from interlayer to the layer and from interlayer Ni cations sharing their coordination O atoms with Ni(Mn) from adjacent layers, most likely accounts for this reduced availability. Increasing the temperature further to 500 °C induces the transformation of Ni10_8y into cryptomelane,

that exhibits larger particle size and improved crystallinity compared to its Ni10_8y birnessite precursor (Figs. 1 and 3). Furthermore, Ni is thoroughly inserted in cryptomelane framework, as evidenced by HAADF-STEM analysis (Fig. 3i), thus providing a dramatically higher stability to this foreign cation. Though not directly relevant to acid leaching or weathering in natural environments, results from acid dissolution experiments might shed light on similar but much less harsh leaching processes in the environment.

5 Conclusions

Crystallinity, morphology, Mn AOS and Ni binding mechanisms are essentially unaffected when aging Ni-doped hexagonal birnessite in the dry state at room temperature for up to 8 years. When heated, the proportion of edge-sharing Ni-Ni(Mn) pairs in aged birenssites increases with temperature increasing from 25-200 ºC before reaching a steady state when increasing the temperature further from 200-400 ºC. Over this whole temperature range, birnessite layer structure is retained and Mn AOS remains constant. At higher temperatures (400-500 ºC), Ni-doped birnessites transform to cryptomelane, Ni doping increasing slightly birnessite stability and delaying the mineral transformation. At 500 ºC, Ni-doped birnessite with an initial Ni/Mn molar ratio of 0.13 fully transforms to cryptomelane, with a minor $NiMnO_3$ impurity. Along this mineral transformation, Mn AOS is sharply increased, Mn cations being essentially Mn^{4+} in the cryptomelane framework, and corner-sharing Mn-Mn(Ni) bond length is decreased. The increasing proportion of edge-sharing Ni-Ni(Mn) pairs in heated birnessite decreases Ni release to solution during reductive acid dissolution, whereas

incorporation of Ni in the cryptomelane framework essentially inhibits this release. These results provide additional insights in the stability of birnessite-like minerals under dry conditions that will most likely become more frequent owing to climate change, and in the geochemical behavior of associated trace metal elements.

Acknowledgements

The authors gratefully thank the Natural Science Foundations of China (Grants 42077015 and 41771267), Key Science and Technology Projects of Inner Mongolia autonomous region (2019ZD001), and the Fundamental Research Funds for the Central Universities (Grant 103-510320036) for financial support.

References

Alvarez M., Rueda E. H. and Sileo E. E. (2006) Structural characterization and chemical reactivity of synthetic Mn-goethites and hematites. *Chem. Geol.* **231**, 288-299.

Alvarez M., Rueda E. H. and Sileo E. E. (2007) Simultaneous incorporation of Mn and Al in the goethite structure. *Geochim. Cosmochim. Acta* **71**, 1009-1020.

Atkins A. L., Shaw S. and Peacock C. L. (2014) Nucleation and growth of todorokite from birnessite: Implications for trace-metal cycling in marine sediments. *Geochim. Cosmochim. Acta* **144**, 109-125.

Atkins A. L., Shaw S. and Peacock C. L. (2016) Release of Ni from birnessite during transformation of birnessite to todorokite: Implications for Ni cycling in marine sediments. *Geochim. Cosmochim. Acta* **189**, 158-183.

Beak D. G., Basta N. T., Scheckel K. G. and Traina S. J. (2008) Linking solid phase speciation of Pb sequestered to birnessite to oral Pb bioaccessibility: implications for soil remediation. *Environ. Sci. Technol.* **42**, 779-785.

Birkner N. and Navrotsky A. (2017) Thermodynamics of manganese oxides: Sodium, potassium, and calcium birnessite and cryptomelane. *Proc. Natl. Acad. Sci. USA* **114**, E1046-E1053.

Cai J., Liu J., Willis W. S. and Suib S. L. (2001) Framework doping of iron in tunnel structure cryptomelane. *Chem. Mater.* **13**, 2413-2422.

Chen C. C., Golden D. C. and Dixon J. B. (1986) Transformation of synthetic birnessite

to cryptomelane: An electron microscopic study. *Clays Clay Miner.* **34**, 565-571.
Ching S., Driscoll P. F., Kieltyka K. S., Marvel M. R. and Suib S. L. (2001) Synthesis of a new hollandite-type manganese oxide with framework and interstitial Cr(III). *Chem. Commun.*, 2486-2487.
Cui H., Qiu G., Feng X., Tan W. and Liu F. (2009) Birnessites with different average manganese oxidation states synthesized, characterized, and transformed to todorokite at atmospheric pressure. *Clays Clay Miner.* **57**, 715-724.
Drits V. A., Lanson B. and Gaillot A. C. (2007) Birnessite polytype systematics and identification by powder X-ray diffraction. *Am. Mineral.* **92**, 771-788.
Drits V. A., Silvester E., Gorshkov A. I. and Manceau A. (1997) Structure of synthetic monoclinic Na-rich birnessite and hexagonal birnessite: I. Results from X-ray diffraction and selected-area electron diffraction. *Am. Mineral.* **82**, 946–961.
Giovanoli R. (1980) Vernadite is random-stacked birnessite. *Mineral. Deposita* **15**, 251-253.
Golden D., Dixon J. and Chen C. (1986) Ion exchange, thermal transformations, and oxidizing properties of birnessite. *Clays Clay Miner.* **34**, 511-520.
Grangeon S., Fernandez-Martinez A., Warmont F., Gloter A., Marty N., Poulain A. and Lanson B. (2015) Cryptomelane formation from nanocrystalline vernadite precursor: a high energy X-ray scattering and transmission electron microscopy perspective on reaction mechanisms. *Geochem. Trans.* **16**, 12.
Grangeon S., Lanson B. and Lanson M. (2014) Solid-state transformation of nanocrystalline phyllomanganate into tectomanganate: influence of initial layer and interlayer structure. *Acta. Crystallogr. B* **70**, 828-838.
Grangeon S., Lanson B., Lanson M. and Manceau A. (2008) Crystal structure of Ni-sorbed synthetic vernadite: a powder X-ray diffraction study. *Mineral. Mag.* **72**, 1279-1291.
Grangeon S., Lanson B., Miyata N., Tani Y. and Manceau A. (2010) Structure of nanocrystalline phyllomanganates produced by freshwater fungi. *Am. Mineral.* **95**, 1608-1616.
Johnston S. G., Burton E. D. and Moon E. M. (2016) Arsenic Mobilization Is Enhanced by Thermal Transformation of Schwertmannite. *Environ. Sci. Technol.* **50**, 8010-8019.
Jothiramalingam R., Viswanathan B. and Varadarajan T. K. (2006) Synthesis and structural characterization of copper incorporated manganese oxide OMS-2 materials synthesized via potassium birnessite. *Mater. Chem. Phys.* **100**, 257-261.
Kabai J. (1973) Determination of specific activation energies of metal oxides and metal oxide hydrates by measurement of the rate of dissolution. *Acta Chim. Acad. Sci. Hung* **78**, 57-73.
Kaur N., Singh B. and Kennedy B. J. (2010) Dissolution of Cr, Zn, Cd, and Pb single- and multi-metal-substituted goethite: relationship to structural, morphological, and dehydroxylation properties. *Clays Clay Miner.* **58**, 415-430.
Kelly S. D., Hesterberg D. and Ravel B. (2008) Analysis of soils and minerals using X-ray absorption spectroscopy. In *Methods of Soil Analysis, Part 5-Mineralogical*

Methods (eds. A. L. Ulrey and R. L. Drees). Soil Science Society of America, Wisconsin. pp. 387-463.

Kim K., Yoon H. I. and Choi W. (2012) Enhanced dissolution of manganese oxide in ice compared to aqueous phase under illuminated and dark conditions. *Environ. Sci. Technol.* **46**, 13160-13166.

Kwon K. D., Refson K. and Sposito G. (2009) On the role of Mn(IV) vacancies in the photoreductive dissolution of hexagonal birnessite. *Geochim. Cosmochim. Acta* **73**, 4142-4150.

Kwon K. D., Refson K. and Sposito G. (2013) Understanding the trends in transition metal sorption by vacancy sites in birnessite. *Geochim. Cosmochim. Acta* **101**, 222-232.

Landers M., Gilkes R. J. and Wells M. A. (2009) Rapid dehydroxylation of nickeliferous goethite in lateritic nickel ore: X-ray diffraction and TEM investigation. *Clays Clay Miner.* **57**, 751-770.

Lanson B., Marcus M. A., Fakra S., Panfili F., Geoffroy N. and Manceau A. (2008) Formation of Zn–Ca phyllomanganate nanoparticles in grass roots. *Geochim. Cosmochim. Acta* **72**, 2478-2490.

Lee S., Xu H., Xu W. and Sun X. (2019) The structure and crystal chemistry of vernadite in ferromanganese crusts. *Acta. Crystallogr. B* **75**, 591-598.

Lee S. H., Kim T. W., Park D. H., Choy J.-H., Hwang S.-J., Jiang N., Park S.-E. and Lee Y.-H. (2007) Single-step synthesis, characterization, and application of nanostructured K_x $Mn_{1-y}Co_yO_{2-\delta}$ with controllable chemical compositions and crystal structures. *Chem. Mater.* **19**, 5010-5017.

Li M., Liu H., Chen T., Wei L., Wang C., Hu W. and Wang H. (2019) The transformation of α-(Al, Fe)OOH in natural fire: Effect of Al substitution amount on fixation of phosphate. *Chem. Geol.* **524**, 368-382.

Liu L., Wang X., Zhu M., Ma J., Zhang J., Tan W., Feng X., Yin H. and Liu F. (2019) The speciation of Cd in Cd–Fe coprecipitates: Does Cd substitute for Fe in goethite structure? *ACS Earth Space Chem.* **3**, 2225-2236.

Liu Y., Li Y., Li Y., Chen N., Ding H., Jin S., Wang C. and Lu A. (2021) Photo-stimulated anoxic reduction of birnessite (δ-MnO_2) by citrate and its fine structural responses: Insights on a proton-promoted photoelectron transfer process. *Chem. Geol.* **561,** 120029.

Lu A. and Li Y. (2015) Reactivity of natural Mn oxide cryptomelane. In *Advances in the Environmental Biogeochemistry of Manganese Oxides* (eds. X. Feng, W. Li, M. Zhu, and D. L. Sparks). American Chemical Society, Washington. pp. 89-106.

Lu A., Li Y., Ding H., Xu X., Li Y., Ren G., Liang J., Liu Y., Hong H., Chen N., Chu S., Liu F., Li Y., Wang H., Ding C., Wang C., Lai Y., Liu J., Dick J., Liu K. and Hochella M. F., Jr. (2019) Photoelectric conversion on Earth's surface via widespread Fe- and Mn-mineral coatings. *Proc. Natl. Acad. Sci. USA* **116**, 9741-9746.

Luo W., Hu W. and Xiao S. (2008) Size effect on the thermodynamic properties of silver nanoparticles. *J. Phys. Chem. C* **112**, 2359-2369.

Manceau A., Lanson M. and Geoffroy N. (2007) Natural speciation of Ni, Zn, Ba, and As in ferromanganese coatings on quartz using X-ray fluorescence, absorption, and diffraction. *Geochim. Cosmochim. Acta* **71**, 95-128.

Manceau A., Lanson M. and Takahashi Y. (2014) Mineralogy and crystal chemistry of Mn, Fe, Co, Ni, and Cu in a deep-sea Pacific polymetallic nodule. *Am. Mineral.* **99**, 2068-2083.

Manceau A., Marcus M. A. and Grangeon S. (2012) Determination of Mn valence states in mixed-valent manganates by XANES spectroscopy. *Am. Mineral.* **97**, 816-827.

Manceau A. and Steinmann S. N. (2021) Nature of high- and low-affinity metal surface sites on birnessite nanosheets. *ACS Earth Space Chem.* **5**, 66-76.

McKenzie R. M. (1971) The synthesis of birnessite, cryptomelane, and some other oxides and hydroxides of manganese. *Mineral. Mag.* **38**, 493-503.

Morgan J. J. (2005) Kinetics of reaction between O2 and Mn(II) species in aqueous solutions. *Geochim. Cosmochim. Acta* **69**, 35-48.

Murphy B. F. and Timbal B. (2008) A review of recent climate variability and climate change in southeastern Australia. *Int. J. Climatol.* **28**, 859-879.

Navrotsky A., Mazeina L. and Majzlan J. (2008) Size-Driven Structural and Thermodynamic Complexity in Iron Oxides. *Science* **319**, 1635-1638.

Peacock C. L. (2009) Physiochemical controls on the crystal-chemistry of Ni in birnessite: genetic implications for ferromanganese precipitates. *Geochim. Cosmochim. Acta* **73,**, 3568-3578.

Peña J., Kwon K. D., Refson K., Bargar J. R. and Sposito G. (2010) Mechanisms of nickel sorption by a bacteriogenic birnessite. *Geochim. Cosmochim. Acta* **74**, 3076-3089.

Perrier N., Gilkes R. J. and Colin F. (2006) Heating Fe oxide-rich soils increases the dissolution rate of metals. *Clays Clay Miner.* **54**, 165-175.

Post J. E. (1999) Manganese oxide minerals: Crystal structures and economic and environmental significance. *Proc. Natl. Acad. Sci. USA* **96**, 3447-3454.

Post J. E. and Appleman D. E. (1988) Chalcophanite, $ZnMn_3O_7 .3H_2O$: New crystal-structure determinations. *Am. Mineral.* **73**, 1401-1404.

Qin Z., Xiang Q., Liu F., Xiong J., Koopal L. K., Zheng L., Ginder-Vogel M., Wang M., Feng X., Tan W. and Yin H. (2017) Local structure of Cu^{2+} in Cu-doped hexagonal turbostratic birnessite and Cu^{2+} stability under acid treatment. *Chem. Geol.* **466**, 512-523.

Ravel B. and Newville M. (2005) ATHENA, ARTEMIS, HEPHAESTUS: data analysis for X-ray absorption spectroscopy using IFEFFIT. *J. Synchrotron Radiat.* **12**, 537-541.

Rehr J. J., Zabinsky S. I. and Albers R. C. (1992) High-order multiple scattering calculations of X-ray-absorption fine structure. *Phys. Rev. Lett.* **69**, 3397-3400.

Rein G., Cleaver N., Ashton C., Pironi P. and Torero J. L. (2008) The severity of smouldering peat fires and damage to the forest soil. *Catena* **74**, 304-309.

Sherman D. M. (2005) Electronic structures of iron(III) and manganese(IV) (hydr)oxide minerals: Thermodynamics of photochemical reductive dissolution

in aquatic environments. *Geochim. Cosmochim. Acta* **69**, 3249-3255.

Silvester E. J., Manceau A. and Drits V. A. (1997) The structure of monoclinic Na-rich birnessite and hexagonal birnessite. Part 2. Results from chemical studies and EXAFS spectroscopy. . *American Mineralogist,* **82**, 962–978.

Simanova A. A. and Pena J. (2015) Time-resolved investigation of cobalt oxidation by Mn(III)-rich delta-MnO_2 using quick X-ray absorption spectroscopy. *Environ. Sci. Technol.* **49**, 10867-10876.

Sinha A. K., Pradhan M. and Pal T. (2013) Morphological evolution of two-dimensional MnO_2 nanosheets and their shape transformation to one-dimensional ultralong MnO_2 nanowires for robust catalytic activity. *J. Phys. Chem. C* **117**, 23976-23986.

Sorensen J. V., Gueguen B., Stewart B. D., Peña J., Rouxel O. and Toner B. M. (2020) Large nickel isotope fractionation caused by surface complexation reactions with hexagonal birnessite. *Chem. Geol.* **537**, 119481.

Sunda W. G. and Huntsman S. A. (1994) Photoreduction of manganese oxides in seawater. *Mar. Chem.* **46**, 133-152.

Tang Q., Jiang L., Liu J., Wang S. and Sun G. (2014) Effect of surface manganese valence of manganese oxides on the activity of the oxygen reduction reaction in alkaline media. *ACS Catal.* **4**, 457-463.

Taylor R., McKenzie R. and Norrish K. (1964) The mineralogy and chemistry of manganese in some Australian soils. *Soil Res.* **2**, 235-248.

Tu S., Racz G. J. and Goh T. B. (1994) Transformations of Synthetic Birnessite as Affected by pH and Manganese Concentration. *Clays Clay Miner.* **42**, 321-330.

Vicente-Serrano S. M., Quiring S. M., Peña-Gallardo M., Yuan S. and Domínguez-Castro F. (2020) A review of environmental droughts: Increased risk under global warming? *Earth-Sci. Rev.* **201**, 102953.

Villalobos M., Toner B., Bargar J. and Sposito G. (2003) Characterization of the manganese oxide produced by pseudomonas putida strain MnB1. *Geochim. Cosmochim. Acta* **67**, 2649-2662.

Wang Y., Benkaddour S., Marafatto F. F. and Pena J. (2018) Diffusion- and pH-dependent reactivity of layer-type MnO_2: Reactions at particle edges versus vacancy sites. *Environ. Sci. Technol.* **52**, 3476-3485.

Webb S. M. (2005) SIXPACK: a graphical user interface for XAS analysis using IFEFFIT. . *Physica Scripta* **T115**, 1011–1014.

Wu Z., Lanson B., Feng X., Yin H., Tan W., He F. and Liu F. (2021) Transformation of the phyllomanganate vernadite to tectomanganates with small tunnel sizes: Favorable geochemical conditions and fate of associated Co. *Geochim. Cosmochim. Acta* **295**, 224-236.

Wu Z., Peacock C. L., Lanson B., Yin H., Zheng L., Chen Z., Tan W., Qiu G., Liu F. and Feng X. (2019) Transformation of Co-containing birnessite to todorokite: Effect of Co on the transformation and implications for Co mobility. *Geochim. Cosmochim. Acta* **246**, 21-40.

Yang P., Lee S., Post J. E., Xu H., Wang Q., Xu W. and Zhu M. (2018) Trivalent manganese on vacancies triggers rapid transformation of layered to tunneled

manganese oxides (TMOs): Implications for occurrence of TMOs in low-temperature environment. *Geochim. Cosmochim. Acta* **240**, 173-190.

Yang P., Post J. E., Wang Q., Xu W., Geiss R., McCurdy P. R. and Zhu M. (2019) Metal adsorption controls stability of layered manganese oxides. *Environ. Sci. Technol.* **53**, 7453-7462.

Yin H., Dai X. X., Zhu M. Q., Li F. H., Feng X. H. and Liu F. (2015) Fe-doped cryptomelane synthesized by refluxing at atmosphere: Structure, properties and photocatalytic degradation of phenol. *J. Hazard. Mater.* **296**, 221-229.

Yin H., Li H., Wang Y., Ginder-Vogel M., Qiu G. H., Feng X. H., Zheng L. R. and Liu F. (2014) Effects of Co and Ni co-doping on the structure and reactivity of hexagonal birnessite. *Chem. Geol.* **381**, 10-20.

Yin H., Tan W. F., Zheng L. R., Cui H. J., Qiu G. H., Liu F. and Feng X. H. (2012) Characterization of Ni-rich hexagonal birnessite and its geochemical effects on aqueous Pb^{2+}/Zn^{2+} and As(III). *Geochim. Cosmochim. Acta* **93**, 47-62.

Zhang Q., Cheng X. D., Qiu G. H., Liu F. and Feng X. H. (2016) Size-controlled synthesis and formation mechanism of manganese oxide OMS-2 nanowires under reflux conditions with $KMnO_4$ and inorganic acids. *Solid State Sci.* **55**, 152-158.

Zhang Q., Xiao Z., Feng X., Tan W., Qiu G. and Liu F. (2011) α-MnO_2 nanowires transformed from precursor δ-MnO_2 by refluxing under ambient pressure: The key role of pH and growth mechanism. *Mater. Chem. Phys.* **125**, 678-685.

Zhu M., Farrow C. L., Post J. E., Livi K. J. T., Billinge S. J. L., Ginder-Vogel M. and Sparks D. L. (2012) Structural study of biotic and abiotic poorly-crystalline manganese oxides using atomic pair distribution function analysis. *Geochim. Cosmochim. Acta* **81**, 39-55.

Zhu Y., Luo Q. and Liu Y. (2022) *Deserts and Desertification*. IntechOpen, London.

Table 1 Nomenclature of hexagonal turbostratic birnessites and their derivatives.

Sample	Dry aging (year)		Thermal treatment of the 8 year aged sample at different temperatures (ºC)						
	5	8	50	100	150	200	300	400	500
HB	HB_5y	HB_8y	HB_8y_50	HB_8y_100	HB_8y_150	HB_8y_200	HB_8y_300	HB_8y_400	HB_8y_500
Ni10	Ni10_5y	Ni10_8y	Ni10_8y_50	Ni10_8y_100	Ni10_8y_150	Ni10_8y_200	Ni10_8y_300	Ni10_8y_400	Ni10_8y_500

Table 2 Ni K-edge EXAFS structural parameters for thermal transformation products of the 8-year aged Ni10 sample.

Shells	Parameters	Ni10_8y	Ni10_8y_50	Ni10_8y_100	Ni10_8y_150	Ni10_8y_200	Ni10_8y_300	Ni10_8y_400
Ni-O_1[a]	R (Å)	2.040(0.006)	2.039(0.006)	2.038(0.007)	2.034(0.007)	2.035(0.007)	2.013(0.007)	2.015(0.009)
	σ^2 (Å)	0.0051(0.0004)	0.0050(0.0004)	0.0051(0.0005)	0.0052(0.0005)	0.0050(0.0005)	0.0061(0.0005)	0.0065(0.0006)
Ni-$Mn_{1,E}$	CN	6×(1-f)[b]	6×(1-f)	6×(1-f)	6×(1-f)	6×(1-f)	6×(1-f)	6×(1-f)
	R (Å)	2.860(0.010)	2.846(0.010)	2.849(0.010)	2.845(0.009)	2.863(0.009)	2.849(0.009)	2.865(0.013)
	σ^2 (Å)	σ^2 (Ni-$Mn_{1,TC}$)	σ^2 (Ni-$Mn_{1,TC}$)	σ^2 (Ni-$Mn_{1,TC}$)	σ^2 (Ni-$Mn_{1,TC}$)	σ^2 (Ni-$Mn_{1,TC}$)	σ^2 (Ni-$Mn_{1,TC}$)	σ^2 (Ni-$Mn_{1,TC}$)
Ni-O_2[a]	R (Å)	3.340(0.065)	3.326(0.046)	3.317(0.039)	3.337(0.059)	3.357(0.103)	3.299(0.046)	3.293(0.052)
	σ^2 (Å)	0.0165(0.0086)	0.0103(0.0052)	0.0062(0.0035)	0.0114(0.0067)	0.0217(0.0143)	0.0105(0.0058)	0.0096(0.0062)
Ni-$Mn_{1,TC}$	CN	6×f	6×f	6×f	6×f	6×f	6×f	6×f
	R (Å)	3.471(0.008)	3.484(0.009)	3.487(0.013)	3.481(0.011)	3.464(0.012)	3.457(0.016)	3.453(0.023)
	σ^2 (Å)	0.0057(0.0005)	0.0050(0.0006)	0.0046(0.0008)	0.0049(0.0007)	0.0063(0.0006)	0.0072(0.0009)	0.0084(0.0013)
Ni-O_3	CN	9×f+12×(1-f)	9×f+12×(1-f)	9×f+12×(1-f)	9×f+12×(1-f)	9×f+12×(1-f)	9×f+12×(1-f)	9×f+12×(1-f)
	R (Å)	4.449(0.025)	4.457(0.025)	4.462(0.023)	4.459(0.026)	4.450(0.060)	4.395(0.030)	4.426(0.051)
	σ^2 (Å)	0.0075(0.0027)	0.0072(0.0026)	0.0054(0.0022)	0.0063(0.0026)	0.0146(0.0082)	0.0094(0.0035)	0.0132(0.0065)
Ni-$Mn_{2,E}$	CN	6×(1-f)	6×(1-f)	6×(1-f)	6×(1-f)	6×(1-f)	6×(1-f)	6×(1-f)
	R (Å)	4.976(0.039)	4.992(0.044)	4.988(0.046)	4.985(0.040)	5.001(0.028)	4.966(0.023)	4.962(0.042)
	σ^2 (Å)	σ^2 (Ni-$Mn_{2,TC}$)	σ^2 (Ni-$Mn_{2,TC}$)	σ^2 (Ni-$Mn_{2,TC}$)	σ^2 (Ni-$Mn_{2,TC}$)	σ^2 (Ni-$Mn_{2,TC}$)	σ^2 (Ni-$Mn_{2,TC}$)	σ^2 (Ni-$Mn_{2,TC}$)
Ni-$Mn_{2,TC}$	CN	6×f	6×f	6×f	6×f	6×f	6×f	6×f
	R (Å)	5.472(0.020)	5.437(0.023)	5.448(0.032)	5.475(0.032)	5.545(0.022)	5.493(0.027)	5.457(0.057)
	σ^2 (Å)	0.0060(0.0018)	0.0065(0.0022)	0.0073(0.0030)	0.0068(0.0027)	0.0035(0.0011)	0.0058(0.0017)	0.0092(0.0039)
	f	**0.735(0.036)**	**0.728(0.039)**	**0.656(0.050)**	**0.628(0.049)**	**0.519(0.045)**	**0.516(0.065)**	**0.489(0.104)**
E0(eV)		-2.5(1.1)	-0.2(1.1)	-2.5(1.2)	0.1(1.2)	-1.8(1.2)	-3.5(1.1)	-3.3(1.5)
Chi Sq		183.54	289.48	256.49	447.79	360.36	249.14	276.41
R factor		0.0229	0.0215	0.0285	0.0291	0.0355	0.0304	0.0409

[a]The coordination numbers of these Ni-O shells are 6. [b]f is the fraction of Ni adsorbed on vacancies as triple corner-sharing complexes (TC) of the total Ni in samples.

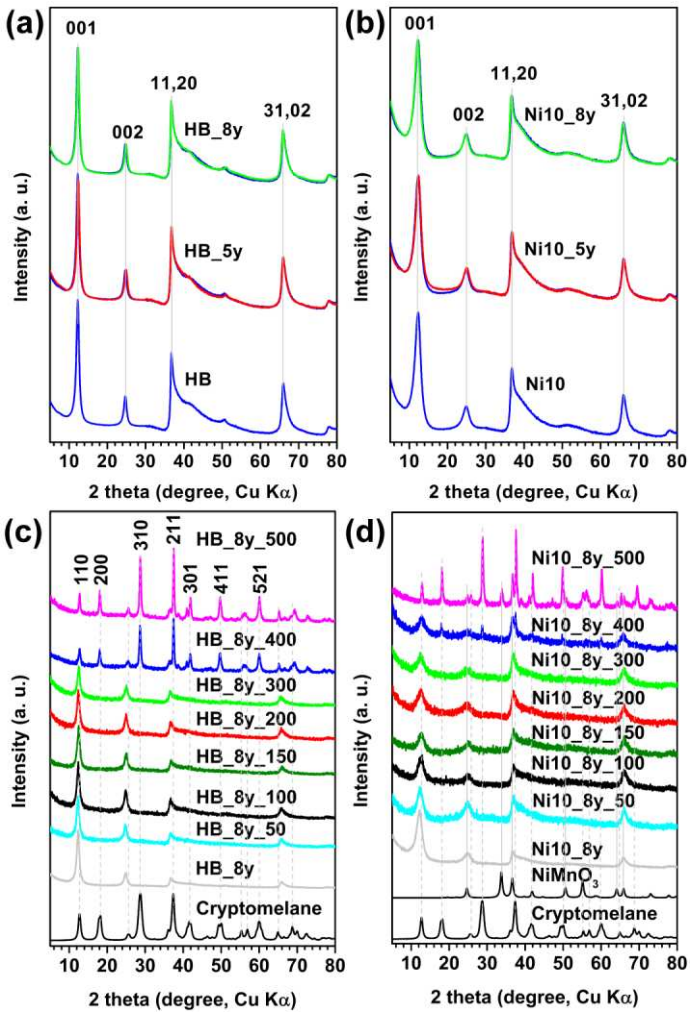

Fig. 1 Powder XRD patterns of pristine and aged turbostratic hexagonal birnessite samples HB (a) and Ni10 (b) for 5 and 8 years at 25 ºC, and of thermal transformation products derived from 8-year aged samples HB_8y (c) and Ni10_8y (d). In panels (a)-(b), the high-angle region (30-80 º 2θ) was scaled by a factor 4 (HB) or 2 (Ni10), and in each series the pristine sample was overlaid to emphasize the evolution of the XRD profiles upon aging. In panels (c)-(d), calculated XRD patterns for cryptomelane (ICDD 74-1451; dashed light gray lines) and NiMn(IV)O_3 (ICDD 75-2089; solid light gray lines) were overlaid to identify the transformation products at high temperatures.

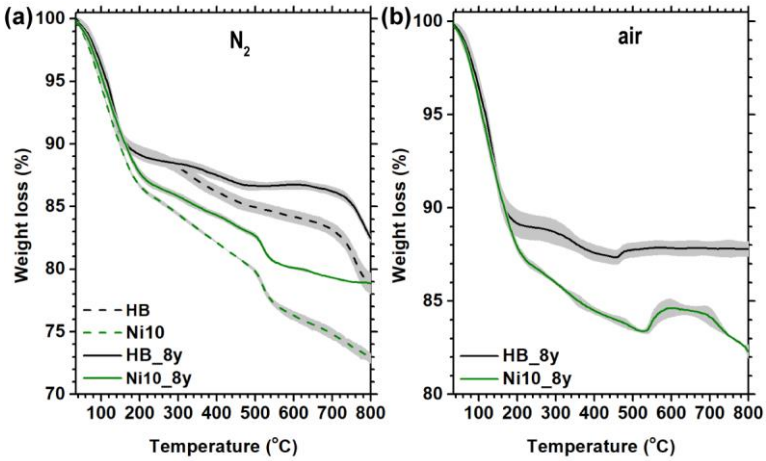

Fig. 2 TGA curves of Ni-free and Ni-doped birnessites before and after aging in dry state at room temperature for 8 years in N_2 atmosphere (a), and those of 8-year aged samples in dry air atmosphere (b). The data for the fresh Ni-doped samples (dashed lines) are from Yin et al. (Yin et al., 2012). For all the samples, the TGA curves are averaged from 2-3 measurements, standard errors being shown as light gray shading.

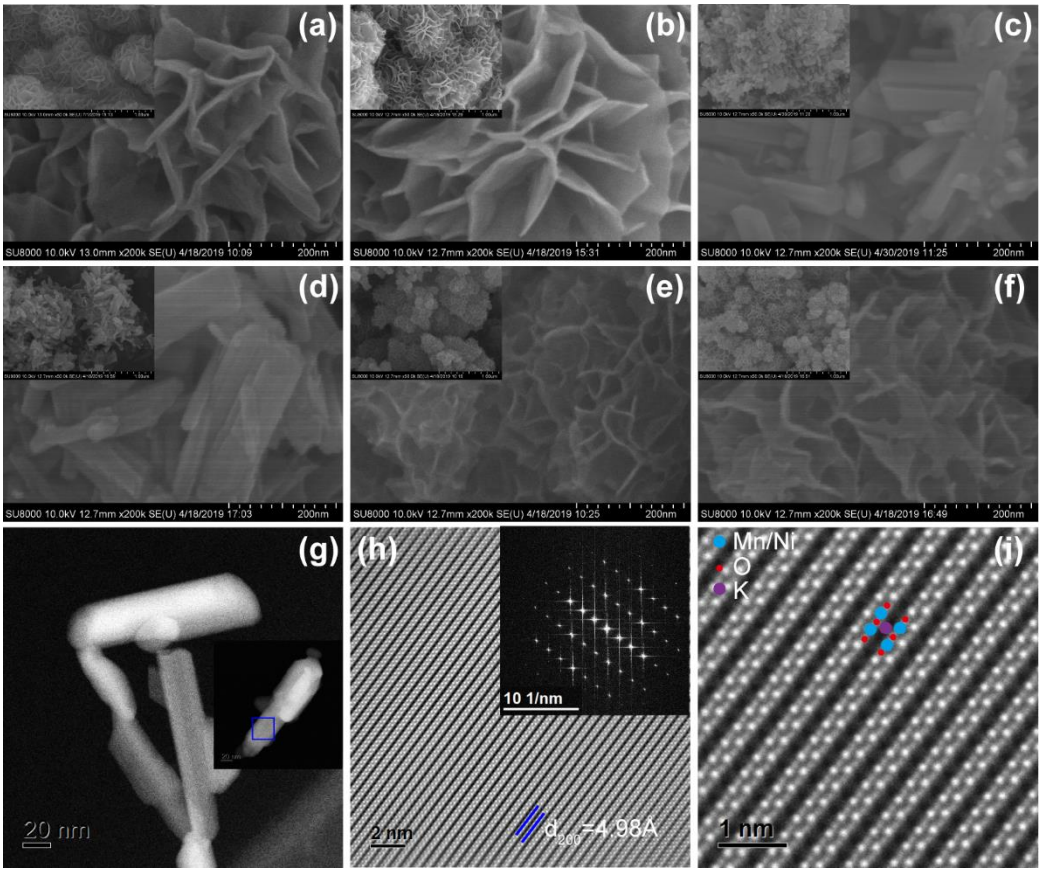

Fig. 3 High magnification FESEM images of HB_8y (a), HB_8y_300 (b), HB_8y_400 (c), HB_8y_500 (d), Ni10_8y (e), and Ni10_8y_400 (f) with the low magnification images in the inset of each panel. TEM image of Ni10_8y_500 (g) with an independent crystal in the inset with an area labeled using a blue bracket for the HAADF-STEM image with FFT in the inset (h) and the atomic resolution image (i).

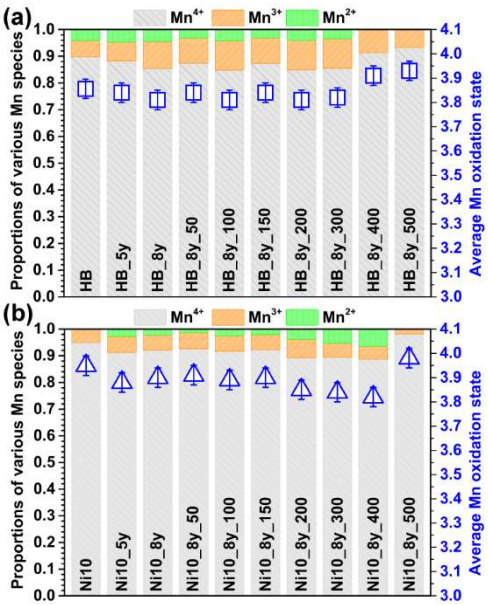

Fig. 4 Proportions of Mn species (Mn^{4+}, Mn^{3+}, and Mn^{2+}) in Ni-free HB (a) and Ni-doped Ni10 (b) birnessite samples after aging at room temperature for 5 and 8 years and in samples derived from heat treatment of the 8-year aged samples at different temperatures, and corresponding variations of the average Mn oxidation state. Data for fresh HB and Ni10 are from Yin et al. (2012).

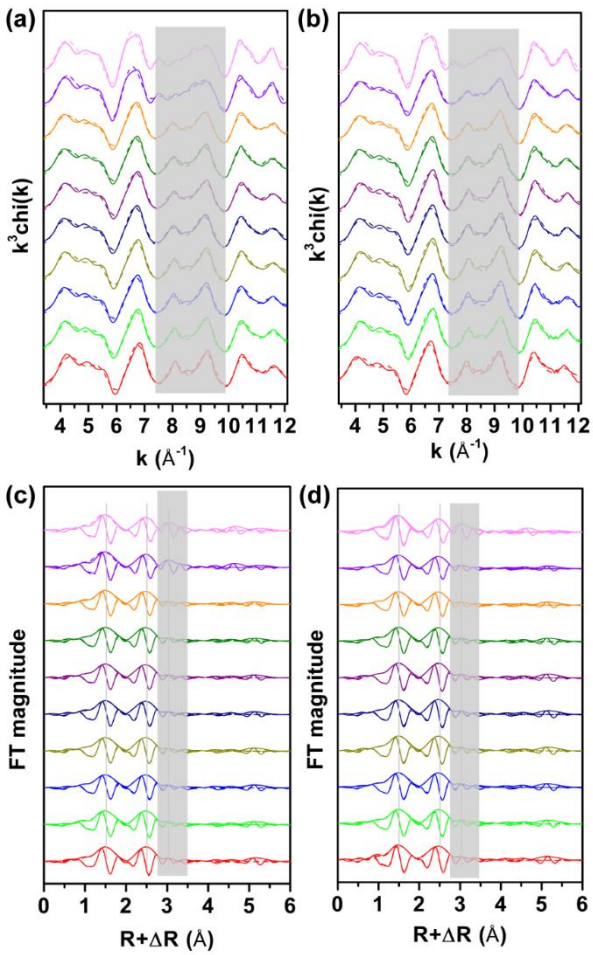

Fig. 5 Mn K-edge k^3-weighted EXAFS spectra (a-b) and corresponding Fourier transforms (c-d) of aged and heat-treated HB (left) and Ni10 (right) birnessite samples. Samples are colored-coded: fresh samples (red), 5-year aged (green), 8-year aged (blue), HB_8y and Ni10_8y samples heated to 50 ºC (dark yellow), 100 ºC (navy), 150 ºC (purple), 200 ºC (olive), 300 ºC (orange), 400 ºC (violet), and 500 ºC (light magenta). Solid and dashed lines are experimental data and their best fits, respectively. All spectra were fitted using a birnessite model derived from Grangeon et al. (2010), except for HB_8y_400, HB_8y_500, and Ni10_8y_500 spectra that were fitted using a cryptomelane model derived from Yin et al. (2015). Light grey bands indicate the main changes in these spectra.

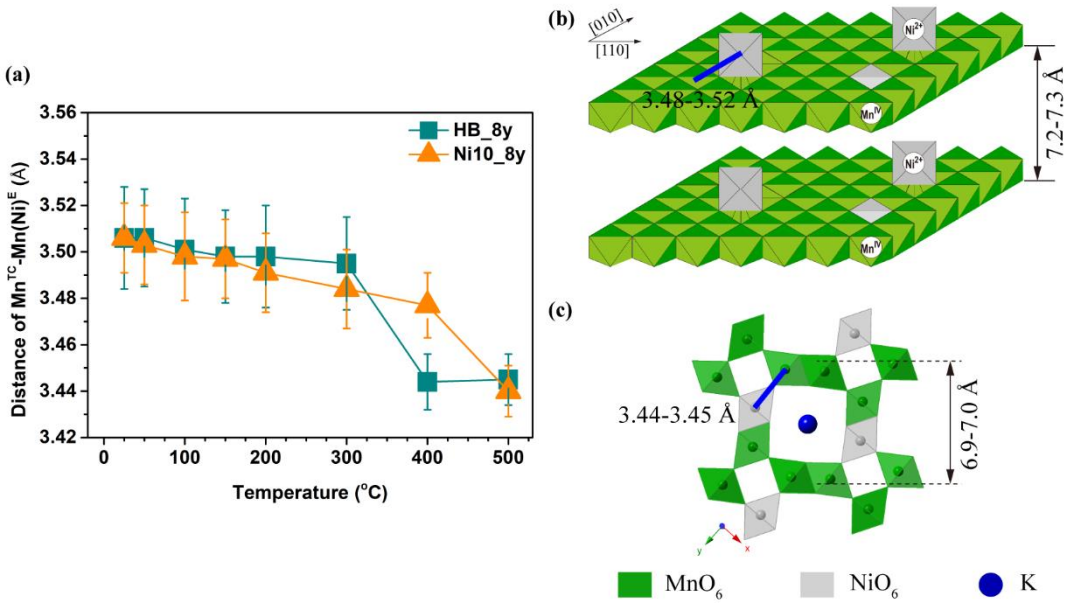

Fig. 6 Evolution as a function of temperature of the EXAFS-derived Mn-Mn(Ni) corner-sharing distances in HB and Ni10 (a), and illustrations of these distances (blue bold solid lines) in the birnessite (b) and cryptomelane (c) structures.

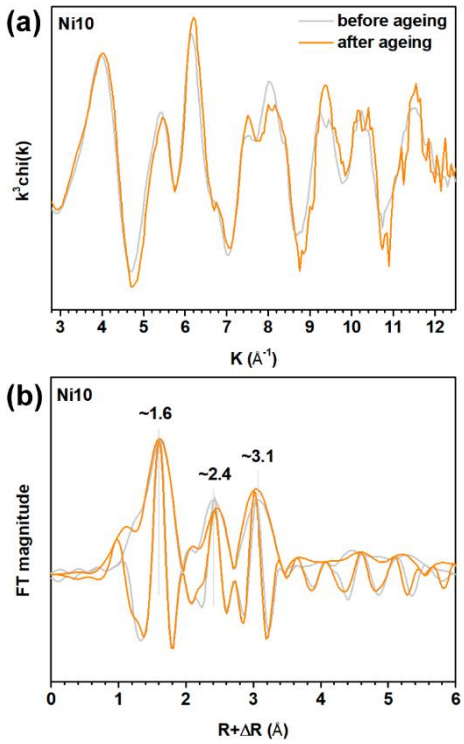

Fig. 7 Nickel K-edge k^3-weighted functions (a) and corresponding Fourier transforms (b) of Ni-doped birnessite samples before (light gray lines) and after (orange lines) dry aging at room temperature for 8 years. Fourier transforms (b) were normalized to the first Ni-O shell (R + ΔR ~1.6 Å).

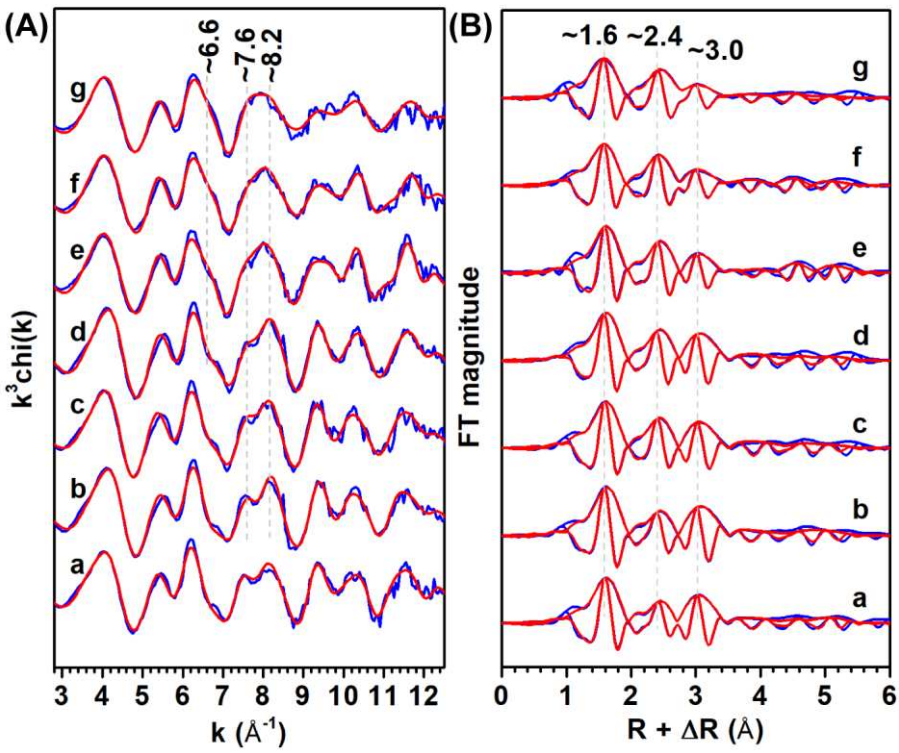

Fig. 8 Nickel K-edge k^3-weighted EXAFS functions (A) and corresponding Fourier transforms (FTs, B) of heat-treated 8-year aged Ni-doped birnessite (Ni10_8y). Experimental data and their best fits are shown as blue and red lines, respectively. Ni10_8y (a), Ni10_8y_50 (b), Ni10_8y_100 (c), Ni10_8y_150 (d), Ni10_8y_200 (e), Ni10_8y_300 (f), and Ni10_8y_400 (g).

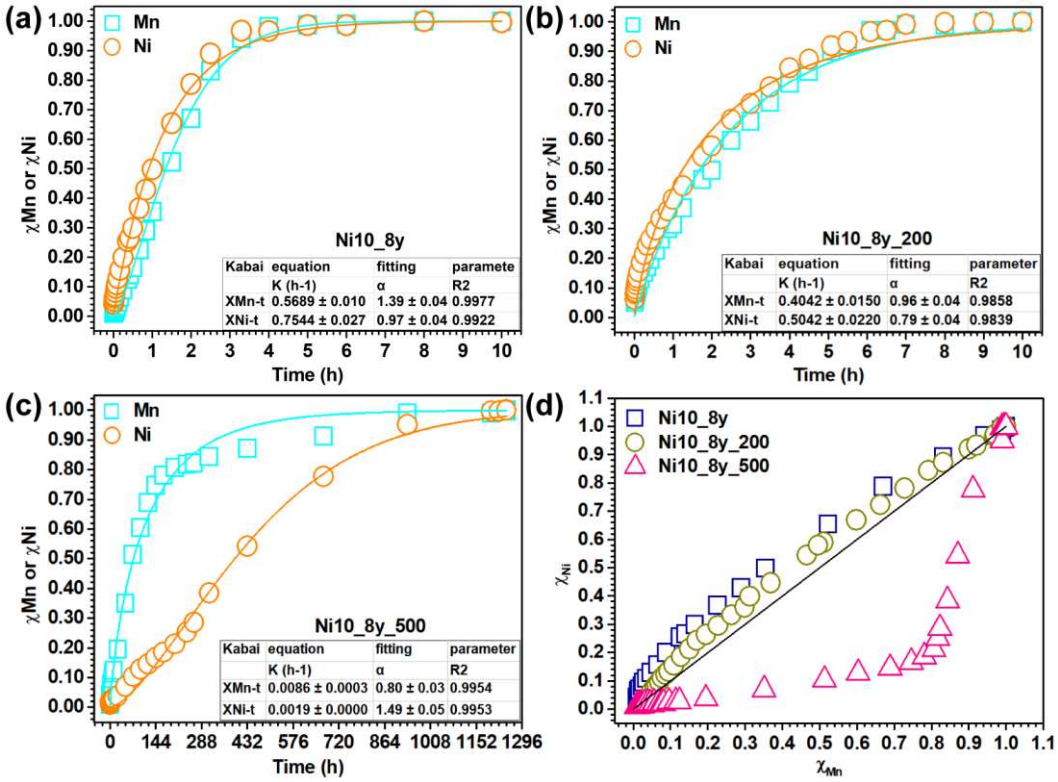

Fig. 9 Releases of Mn and Ni as a function of time along reductive acid dissolution (2 M HCl solution at 37 ºC) of Ni10_8y (a), Ni10_8y_200 (b) and Ni10_8y_500 (c), and corresponding %Ni dissolved (χ_{Ni}) versus %Mn dissolved (χ_{Mn}) curves (d). χ_{Mn} and χ_{Ni} are normalized to the final concentration after complete dissolution. In panels a, b and c, the solid lines are the best fit to the dissolution curve using Kabai equation (Kabai, 1973). Fitting parameters are also listed in tables inserted in the panels. In panel d, the solid black line is the 1:1 line.

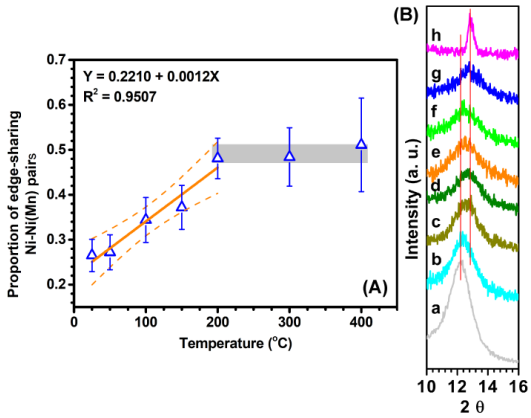

Fig. 10 Evolution of the proportion of edge-sharing Ni-Ni(Mn) pairs as a function of temperature for heat-treated Ni10_8y (A), and shift of the first peak position for heat-treated Ni10_8y (B): Ni10_8y (a), Ni10_8y_50 (b), Ni10_8y_100 (c), Ni10_8y_150 (d), Ni10_8y_200 (e), Ni10_8y_300 (f), Ni10_8y_400 (g), and Ni10_8y_500 (h).